Human Molecular Genetics, 2011, Vol. 20, No. 3 ***482–496***
doi:10.1093/hmg/ddq494
Advance Access published on November 15, 2010

NPHP4 is necessary for normal photoreceptor ribbon synapse maintenance and outer segment formation, and for sperm development

Jungyeon Won[1], Caralina Marín de Evsikova[1], Richard S. Smith[1], Wanda L. Hicks[1], Malia M. Edwards[1], Chantal Longo-Guess[1], Tiansen Li[2], Jürgen K. Naggert[1] and Patsy M. Nishina[1,*]

[1]The Jackson Laboratory, 600 Main Street, Bar Harbor, ME 04609, USA and [2]Massachusetts Eye and Ear Infirmary, Boston, MA 02114, USA

Received August 31, 2010; Revised and Accepted November 10, 2010

Nephronophthisis (NPHP) is an autosomal recessive kidney disease that is often associated with vision and/or brain defects. To date, 11 genes are known to cause NPHP. The gene products, while structurally unrelated, all localize to cilia or centrosomes. Although mouse models of NPHP are available for 9 of the 11 genes, none has been described for nephronophthisis 4 (*Nphp4*). Here we report a novel, chemically induced mutant, *nmf192*, that bears a nonsense mutation in exon 4 of *Nphp4*. Homozygous mutant *Nphp4*$^{nmf192/nmf192}$ mice do not exhibit renal defects, phenotypes observed in human patients bearing mutations in *NPHP4*, but they do develop severe photoreceptor degeneration and extinguished rod and cone ERG responses by 9 weeks of age. Photoreceptor outer segments (OS) fail to develop properly, and some OS markers mislocalize to the inner segments and outer nuclear layer in the *Nphp4*$^{nmf192/nmf192}$ mutant retina. Despite NPHP4 localization to the transition zone in the connecting cilia (CC), the CC appear to be normal in structure and ciliary transport function is partially retained. Likewise, synaptic ribbons develop normally but then rapidly degenerate by P14. Finally, *Nphp4*$^{nmf192/nmf192}$ male mutants are sterile and show reduced sperm motility and epididymal sperm counts. Although *Nphp4*$^{nmf192/nmf192}$ mice fail to recapitulate the kidney phenotype of NPHP, they will provide a valuable tool to further elucidate how NPHP4 functions in the retina and male reproductive organs.

INTRODUCTION

Nephronophthisis (NPHP) is a leading cause of heritable kidney disease in children and young adults. The major clinical features of this autosomal recessive disorder include polyuria, polydipsia and anemia (1–3). End-stage renal failure, characterized by renal fibrosis, medullary cysts and disruption of the basement membrane, occurs during childhood (4). NPHP has been associated with syndromes such as Senior–Loken syndrome (SLSD) with retinitis pigmentosa (RP), Joubert syndrome with RP, cerebellar and brainstem malformations and mental retardation (2).

Mutations in *NPHP1–9, NPHP11* and *AH1* are currently reported to cause NPHP in humans. The proteins encoded by these 11 genes are diverse in structure and cellular localization (3). A mutation in *NPHP4,* which encodes a 1426 amino acid protein named nephrocystin-4, also known as nephroretinin, was first identified in 2002 (5). NPHP4 is a phylogentically conserved protein with no recognized motifs, except for a proline-rich domain between amino acids 458–514. NPHP1, RP GTPase regulator interacting protein 1 (RPGRIP1), NPHP8 (also known as RPGRIP1L) and Retinitis pigmentosa GTPase regulator (RPGR) are reported to be binding partners of NPHP4 (5–8). The N-terminus (amino acids 1–176) of NPHP4 binds to the C-terminal end of NPHP1, to the C2 domain of RPGRIP1 (amino acids 560–590), to the central portion of NPHP8 (amino acids 591–1093) and to the RCC1-like domain of RPGR. NPHP4 has also been identified as part of a protein complex including breast cancer anti-estrogen resistance 1, protein tyrosine kinase 2β and NPHP1

*To whom correspondence should be addressed at: The Jackson Laboratory, 600 Main Street, Bar Harbor, ME 04609, USA. Tel: +1 2072886383; Fax: +1 2072886077; Email: patsy.nishina@jax.org

(9), proteins known to be involved in common renal diseases. NPHP4 localizes in the organelles associated with the centrosomes and primary cilia in cultured MDCK cells (9), and various structures within the retina (6).

In this study, we report a new mouse model of *Nphp4* generated by ethyl nitrosourea (ENU) mutagenesis at the Neuromutagenesis Facility (NMF) of The Jackson Laboratory (JAX). *nmf192* mutants, herein referred to as *Nphp4*$^{nmf192/nmf192}$, bear a nonsense point mutation in the *Nphp4* gene. Contrary to our expectations, *Nphp4*$^{nmf192/nmf192}$ mice do not display overt kidney defects. Instead, *Nphp4*$^{nmf192/nmf192}$ mice exhibit defective outer segment morphogenesis associated with rapid photoreceptor degeneration and male infertility. Since NPHP is often associated with retinal disease in syndromic cases in humans, this mouse model will provide a new resource for examining the tissue-specific phenotypes associated with *NPHP4* mutations.

RESULTS

Nphp4$^{nmf192/nmf192}$ mice exhibit retinal abnormalities but not renal or hearing abnormalities

The *nmf192* mutation, mapped to Chromosome 4 (Supplementary Material, Fig. S1), is a single base pair substitution (T to A) found in exon 4 of the *Nphp4* gene (Fig. 1A). To determine whether the base substitution was novel or a single nucleotide polymorphism shared among strains, a sequence comparison of exon 4 of the *Nphp4* gene from 13 inbred strains was done. All of the examined strains harbored a thymidine at nucleotide 655 (data not shown), indicating that the point mutation was specific to *nmf192/nmf192* mutants. The mutation is predicted to cause amino acid Leu104 to become a termination codon. Leu104 is evolutionarily conserved across species from humans to mouse (Supplementary Material, Fig. S1) (10). A ~150 kDa NPHP4 band was not detected in *Nphp4*$^{nmf192/nmf192}$ mutant retinas (Fig. 1B) by western analysis with an antibody raised against N-terminal 188 amino acids of NPHP4. Besides the ~150 kDa product, multiple smaller bands were observed by western analyses. The smaller bands were found in both mutant and control retinas suggesting non-specific binding or the presence of alternative splice forms of NPHP4 that were not affected by the mutation. In the Ensemble database, Build 37, a shorter isoform of *Nphp4* was reported (transcript ID ENSMUST00000047943), which utilizes alternative exons 4–6 that are not expected to be affected by the *nmf192* mutation. Also, by RT–PCR with a forward primer in exon 2 and reverse primer in intron 3, a ~600 bp major band was observed in both wild-type (WT) and *Nphp4*$^{nmf192/nmf192}$ mutant eyes. Direct sequencing of the amplicon indicated a novel alternative isoform, which extends exon 3 (Supplementary Material, Fig. S1). To date, 12 isoforms in human *NPHP4* (GRCh37) have been posted in the Ensembl database.

Given the disease phenotype observed in patients with *NPHP4* mutations, we examined renal parameters in *Nphp4*$^{nmf192/nmf192}$ mice. The lifespan of *Nphp4*$^{nmf192/nmf192}$ mutants was comparable with WT controls with no evident clinical symptoms of kidney failure (data not shown). Kidney size and weight was similar between mutant and WT controls (data not shown). Kidney cysts, a common feature

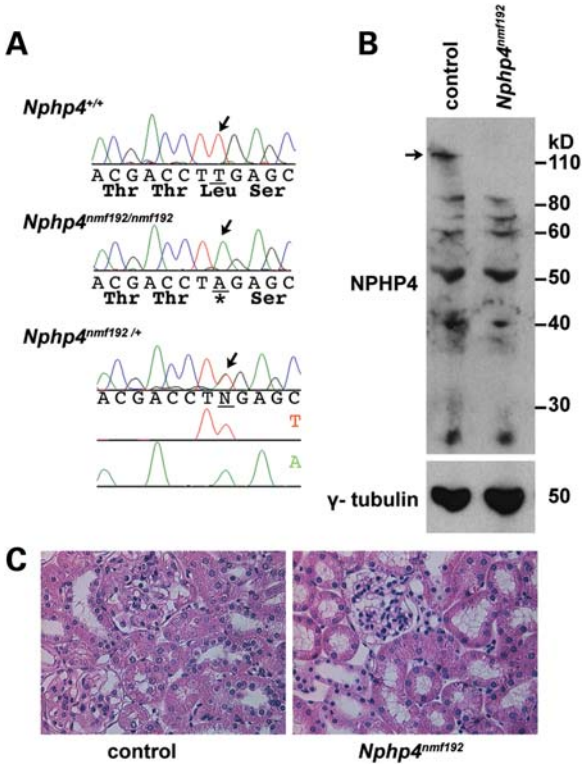

Figure 1. The kidney morphology in *Nphp4*$^{nmf192/nmf192}$ is normal despite the nonsense Leu104Ter mutation. (**A**) By direct sequence analysis, a single base pair substitution (T to A) was found in exon 4 of the *Nphp4* gene of *nmf192/nmf192* mice. The mutation is predicted to cause amino acid Leu104 to become a termination codon. (**B**) To examine the effects of the mutation on the *Nphp4* gene product, an antibody was raised against 188 amino acids from the N-terminus of NPHP4. Western analysis of retinal lysates from 2-month-old control and mutant mice stained with anti-NPHP4 was conducted. Besides a major full size product at ~150 kDa, multiple smaller bands were observed in lysates from control retinas. The largest NPHP4 band was not detected in *Nphp4*$^{nmf192/nmf192}$ mutant retinas, however, smaller bands were found in both mutant and control retinas suggesting alternative splice forms or non-specific interaction with the polyclonal NPHP4 antibody. Staining with anti-γ-tubulin served as a loading control. (**C**) *Nphp4*$^{nmf192/nmf192}$ mice have normal kidney morphology. H&E staining of kidneys from 6-month-old male control (left) and *Nphp4*$^{nmf192/nmf192}$ (right) mice. Bar = 50 μm.

of NPHP, were not detected in *Nphp4*$^{nmf192/nmf192}$ mice even at 2 years of age. Blood urea nitrogen and urine creatinine biochemistries (Supplementary Material, Table S1), indicators of kidney function, were within normal levels and comparable with WT controls. Kidney histology was similar for both WT and mutant mice (Fig. 1C and Supplementary Material, Fig. S1).

Cilia dysfunction can lead to hearing impairment as cilia line the inner hair cells. Examples of cilia-related genetic syndromes, such as BBS (11) and Usher syndrome (12), have been shown to cause both vision and hearing defects. Therefore, hearing in *Nphp4*$^{nmf192/nmf192}$ mice and littermate controls was assessed by auditory brain-stem response (ABR) threshold testing at 2 and 6 months of age (m). At 2m, hearing in *Nphp4*$^{nmf192/nmf192}$ mice was comparable with controls in all ranges tested (data not shown). At 6m, although mutant mice showed an elevated threshold at 32 kHz, the highest frequency tested (average ± standard error; *Nphp4*$^{nmf192/nmf192}$ mice 87.7 ± 4.4 dB; 45 dB is considered to be normal at this frequency), controls were similarly elevated (90.0 ± 5.0 dB).

This suggests that the observed hearing impairment might be due to a general background strain effect associated with aging (13) and not to the *Nphp4*$^{nmf192/nmf192}$ mutation *per se.*

By indirect ophthalmoscopy, the retinas of homozygous *Nphp4*$^{nmf192/nmf192}$ mice appear mottled and grainy with attenuated blood vessels as early as 6 weeks of age (w) and exhibit patches of depigmentation by 10w (Fig. 2A). Histologically, retinas of *Nphp4*$^{nmf192/nmf192}$ mice show progressive photoreceptor degeneration. Outer segments (OS) in mutant mice are shorter than controls as early as 2w (Fig. 1B). At P19, the thickness of outer nuclear layer (ONL) was 43% that of control while the inner nuclear layer (INL) was spared (Fig. 2B–D and Supplementary Material, Fig. S2). By P21, the thickness of the ONL was reduced to 17% of control, and the thickness of INL was reduced to 70% of control. The reduction in the INL, therefore, is likely to be a secondary effect of photoreceptor loss on INL cell viability. Thickness of the outer plexiform layer (OPL) was also remarkably reduced by 4w. The loss of photoreceptor cells occurs as a result of apoptosis (Supplementary Material, Fig. S2). Partial loss of retinal pigment epithelial (RPE) cells was also observed at 10w (data not shown), corresponding to the depigmented patches seen by fundus examination. Electroretinograms (ERG) recorded in 9w mutant mice demonstrate a complete lack of both rod and cone response to light stimuli (Supplementary Material, Fig. S2).

Because photoreceptors were observed to rapidly degenerate in homozygous *Nphp4*$^{nmf192/nmf192}$ mice after eye opening at P14, and *Nphp4* is located in one of the quantitative trait loci (QTLs) regions that harbor gene(s) that lead to sensitivity to light-induced photoreceptor degeneration in mice bearing the *Rpe65* Leu450 mutation (14), we bred *Nphp4*$^{nmf192/nmf192}$ mice in the dark and examined their disease progression histologically. As dark rearing did not retard photoreceptor loss in mutant mice (data not shown), this indicates that the C57BL/6J (B6)-*Nphp4*$^{nmf192/nmf192}$ is not modulated by environmental light exposure.

In order to determine whether the BALB/cJ and 129S1/SvImJ (129) alleles of *Nphp4* might be responsible for the light-sensitivity QTL in *Rpe65* Leu450 mice (14), we examined the entire coding region of *Nphp4* in the 129 and BALB/CJ strains by direct sequencing. BALB/cJ, the strain that is most sensitive to light-induced photoreceptor degeneration, had an identical coding region sequence with B6 (data not shown). Two previously reported nucleotide polymorphisms in the coding region of *Nphp4* were found between strains 129 and B6. One SNP is predicted to cause a non-synonymous change from Thr490 to Ile490, and the other, a synonymous change in Asn620. In order to determine whether the identified SNPs might be responsible for the modulation of the damage caused by light exposure, B6-*Nphp4*$^{nmf192/nmf192}$ mice were out-crossed with 129 mice bearing the *Nphp4* SNPs. While the ONL thickness (ONLT) of central retina was shortened in the parental 129 strain 2 weeks after exposure to bright light (12 000 lux, 1 h exposure), the retina of B6;129-*Nphp4*$^{+/nmf192}$ F1 mice, treated in the same manner, were not affected and were similar to B6 control mice (data not shown).

Taken together, the disease progression of the B6-*Nphp4*$^{nmf192/nmf192}$ allele was not modulated by dark rearing, and the light sensitive QTL in *Rpe65* Leu450 mice identified in the BALB/cJ and 129 strains is not caused by coding region alterations in *Nphp4*.

OS do not form properly in *Nphp4*$^{nmf192/nmf192}$ mice

To better assess the effects of the shortened OS structure in the *Nphp4*$^{nmf192/nmf192}$ retina, the localization of rod OS proteins, rhodopsin and ROM1 was examined. Both proteins were found to mislocalize to inner segments (IS) and ONL (Fig. 3A–D and Supplementary Material, Fig. S3). Cone opsins mislocalized to the IS and ONL but were also found in OS-like structures, as viewed from a scleral orientation of whole-mount retinas from P14 *Nphp4*$^{nmf192/nmf192}$ mice (Fig. 3E and F).

NPHP4 was previously localized to the connecting cilia (CC) region in mouse retina (6). We examined NPHP4 localization in respect to the axonemal marker, RP1, and basal body marker, γ-tubulin (Fig. 4A–D). NPHP4 staining, which could be blocked by competing with a recombinant N-terminal NPHP4 fragment, was found in the transition zone of the CC between the axoneme and the basal bodies. This suggests a structural or transport role for NPHP4. We, therefore, examined the translocation of transducin and arrestin, signaling proteins that traverse the CC upon light exposure. As expected, in controls, transducin localized to OS in dark-adapted retinas and translocated to the IS upon light exposure, with the converse being true for arrestin (Fig. 4E, F, I and J). In dark-adapted retinas from *Nphp4*$^{nmf192/nmf192}$ mice, transducin staining was observed in both the IS and OS (Fig. 4G), indicating a partial mislocalization. However, upon light stimulus, the transducin in the OS translocated to the IS (Fig. 4H). Arrestin immunostaining was limited to the IS in dark-adapted retinas as in controls, and as anticipated, translocated to the OS upon light stimulation (Fig. 4K and L). NPHP4, therefore, does not appear to be necessary for light-dependent protein translocation across the CC. Staining pattern and intensity of intraflagellar transport protein, IFT88 (also known as polaris), involved in active transport across the CC was similar in *Nphp4*$^{nmf192/nmf192}$ and control retinas (Supplementary Material, Fig. S3B). Also, no obvious abnormalities in the staining pattern of acetylated tubulin in mutant retina were noted (Fig. 4M and N). This, taken together with the normal staining appearance of RP1 and γ-tubulin, suggests that the CC structure is intact in mutant retinas. In contrast, the staining patterns of RPGRIP1 and RPGR, proteins normally localized to the outer sheath of the CC, were aberrant in *Nphp4*$^{nmf192/nmf192}$ mice. Anti-RPGRIP1 and anti-RPGR staining of the CC was significantly reduced in mutant retina compared with controls (Fig. 4O and P and Supplementary Material, Fig. S3) and appeared to be partially mislocalized to the ONL as indicated by both the diffuse and the areas of bright linear staining in the photoreceptor cytoplasm surrounding the nuclei. The levels of both proteins, however, were not reduced in the mutant eye when assessed by western analysis (Supplementary Material, Fig. S3), suggesting that NPHP4 may be, in part, necessary for the CC localization of RPGRIP1 and RPGR.

Given the localization of NPHP4, we examined the morphological features of the OS and CC in greater detail by transmission electron microscopy (TEM) and scanning electron

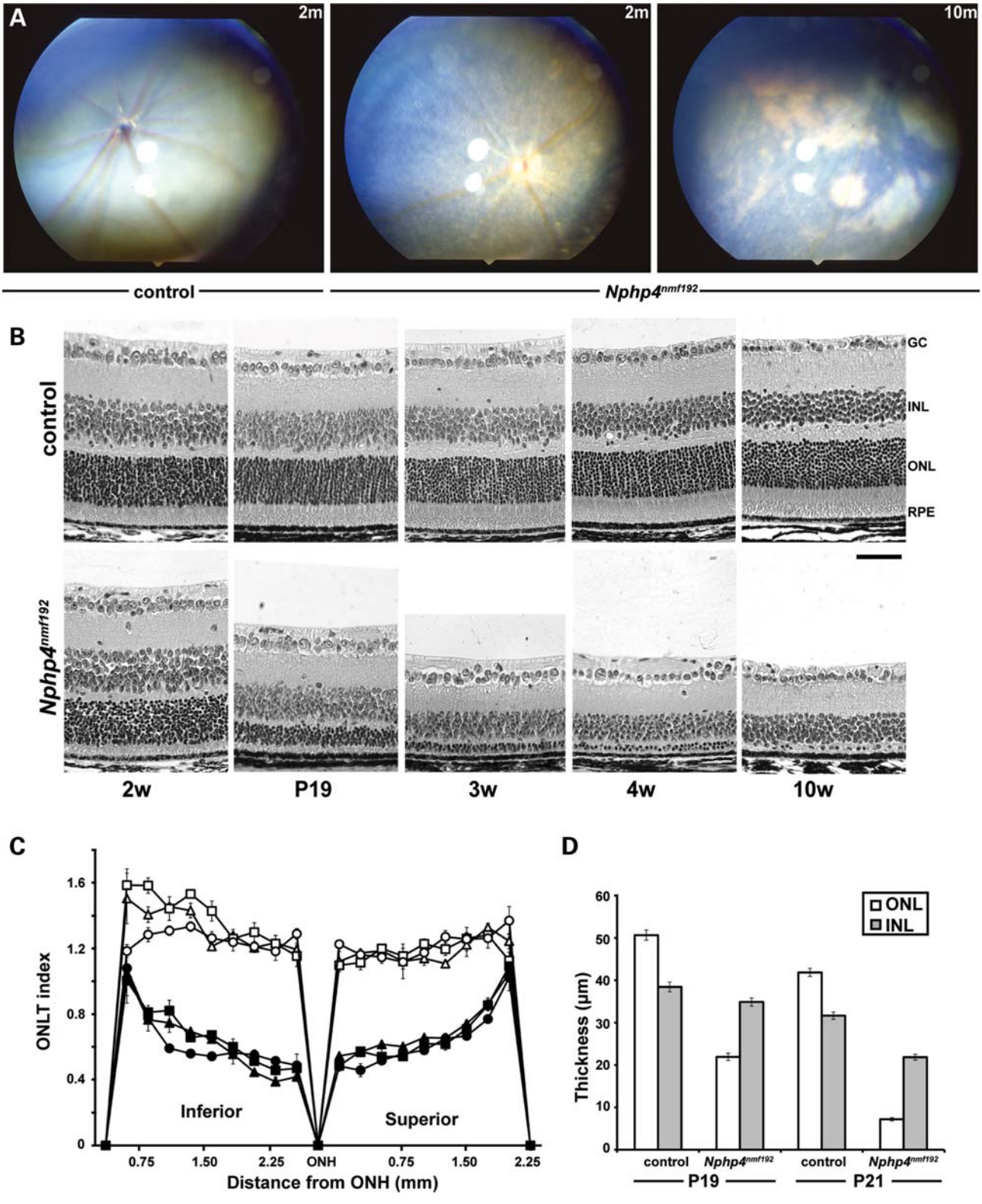

Figure 2. Longitudinal studies examining photoreceptor degeneration. (**A**) Fundus photographs of *Nphp4*$^{nmf192/nmf192}$ mice at 2 and 10m with littermate control at 2m. Retinas of *Nphp4*$^{nmf192/nmf192}$ mutants appear grainy with large patches of depigmentation. (**B**) *Nphp4*$^{nmf192/nmf192}$ mutant retinas show thin OS at 2w without a notable ONL reduction, whereas at 4w only one layer of cell bodies remained in the ONL. (**C**) Pan-retinal ONLT index ($\pm$SEM) was obtained from three retinas each of control (open symbols) and of mutant (closed symbols) mice. In the central retina, ONLT index of mutants were significantly reduced. (**D**) Average retinal thickness ($\pm$SEM) of the ONL and the INL of control and mutant mice at P19 and P21. $n = 5$. GC, ganglion cell layer; INL, inner nuclear layer; OPL, outer plexiform layer; IS, inner segment; ONL, outer nuclear layer; RPE, retinal pigmented epithelium. Bar = 50 μm.

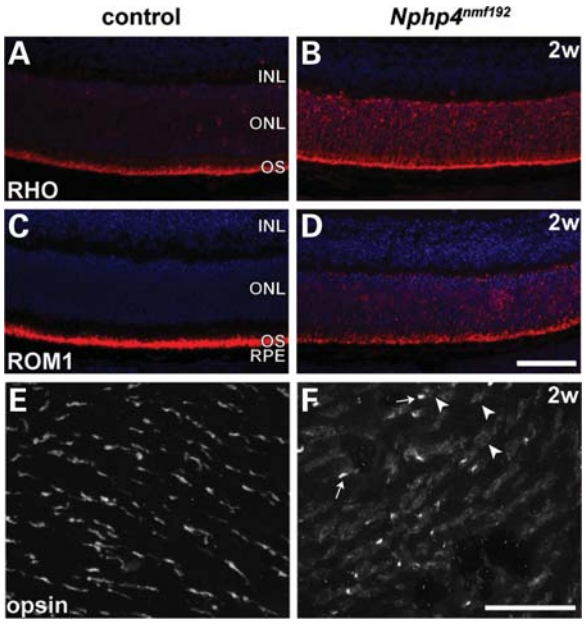

Figure 3. Mislocalization of OS proteins. Rhodopsin (RHO; **A** and **B**) and ROM1 (**C** and **D**) mislocalized to the IS and ONL in retinas from 2-week-old mice. By whole-mount staining, the majority of green opsin was found to mislocalize to the IS and ONL in *Nphp4*$^{nmf192/nmf192}$ retina (**E** and **F**). However, staining was also found in the OS-like structures. OS, outer segment. Bars = 50 μm.

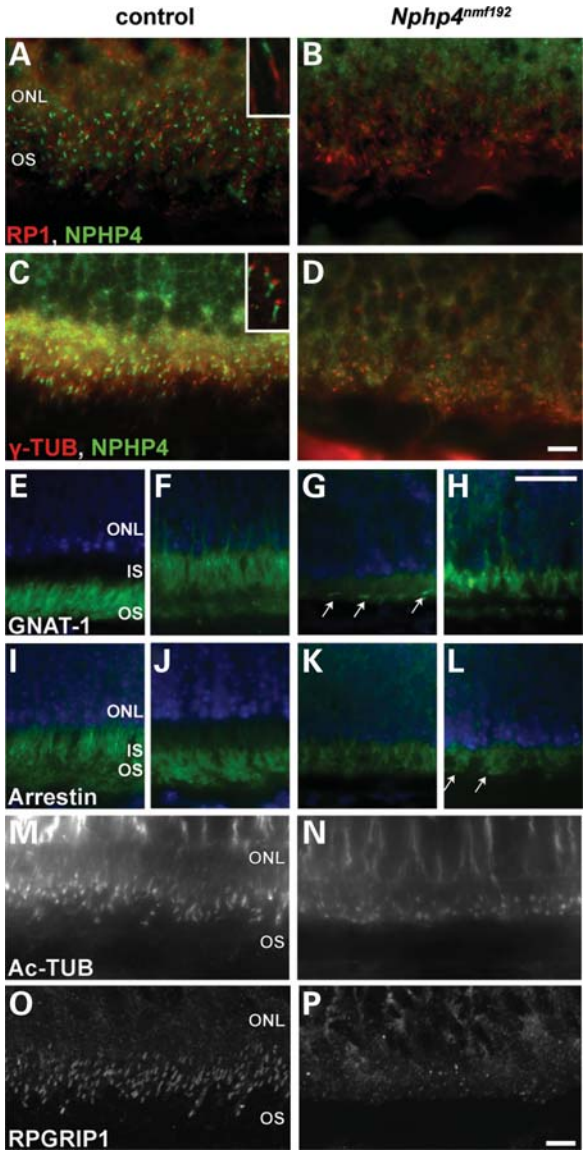

Figure 4. NPHP4 localization and CC marker analysis. NPHP4 localization was examined by co-staining with RP1 (**A** and **B**) and γ-tubulin (γ-TUB; **C** and **D**). Insets represent ×6 magnified images. NPHP4 staining was not detected in *Nphp4*$^{nmf192/nmf192}$ CC, whereas RP1 and γ-tubulin were similar to that observed in controls (B and D). Photo-transduction of rod-transducin (GNAT-1; **E**–**H**) and arrestin (**I**–**L**) in dark-adapted (E, G, I, K) and light-stimulated (F, H, J, L) conditions. Arrows indicate OS in *Nphp4*$^{nmf192/nmf192}$ retina. The localization of acetylated tubulin (Ac-TUB; **M** and **N**) and RPGRIP1 (**O** and **P**) were examined. All retinal sections were obtained at P14. Bars = 20 μm (A–L).

microscopy (SEM). TEM confirmed the shorter OS observed by light microscopy at P14 in mutant retinas. In addition, TEM revealed that the OS were disorganized, and reduced in number when compared with littermate controls, which displayed uniformly orientated and elongated OS (Fig. 5A and B). Basal bodies and axonemes were similar in structure in *Nphp4*$^{nmf192/nmf192}$ mice and in controls (Fig. 5 and Supplementary Material, Fig. S4); however, the distal end of mutant CC flanged outwardly to a greater degree than in WT (Supplementary Material, Fig. S4). By SEM, P7 mutant retinas were similar in morphology to littermate controls (Fig. 5C and D). Nascent cilia emerged from IS, and the length and number of cilia of *Nphp4*$^{nmf192/nmf192}$ mice were comparable with that of controls. At this age, control, but not mutant mice, occasionally exhibited rudimentary OS at the CC tip (15). At P12, control OS were elongated and formed paddle-shaped structures, consistent with earlier observations reported in the literature (15,16). In mutant retinas, however, rudimentary OS were rarely observed and OS failed to elongate (Fig. 5E and F).

Synaptic defects in the OPL of *Nphp4*$^{nmf192/nmf192}$ mutant retina

The onset and basis for the shortened OPL of mutant animals observed by light microscopy was examined in further detail. While the thickness of the OPL in *Nphp4*$^{nmf192/nmf192}$ mutant retinas was not obviously different from controls by light microscopy at P10, by P11 the difference was readily apparent (Fig. 6A). As shown in Figure 1, by P14 the OPL thickness in mutants was approximately 50% that of controls and by 4w, ~25% of controls.

Immunohistochemical (IHC) analysis of the OPL was carried out to determine whether particular synaptic proteins were affected in *Nphp4*$^{nmf192/nmf192}$ mutants. At P8, staining of synaptophysin, a major synaptic vesicle protein, was similar in mutants and controls (Fig. 6B). However, by P12 the continuous linear staining within the OPL, normally observed in WT mice, was disrupted in *Nphp4*$^{nmf192/nmf192}$ retinas with focal areas of brightly staining aggregates surrounded by areas devoid of staining. Some synaptophysin positive ectopic synapses were detected deep within the

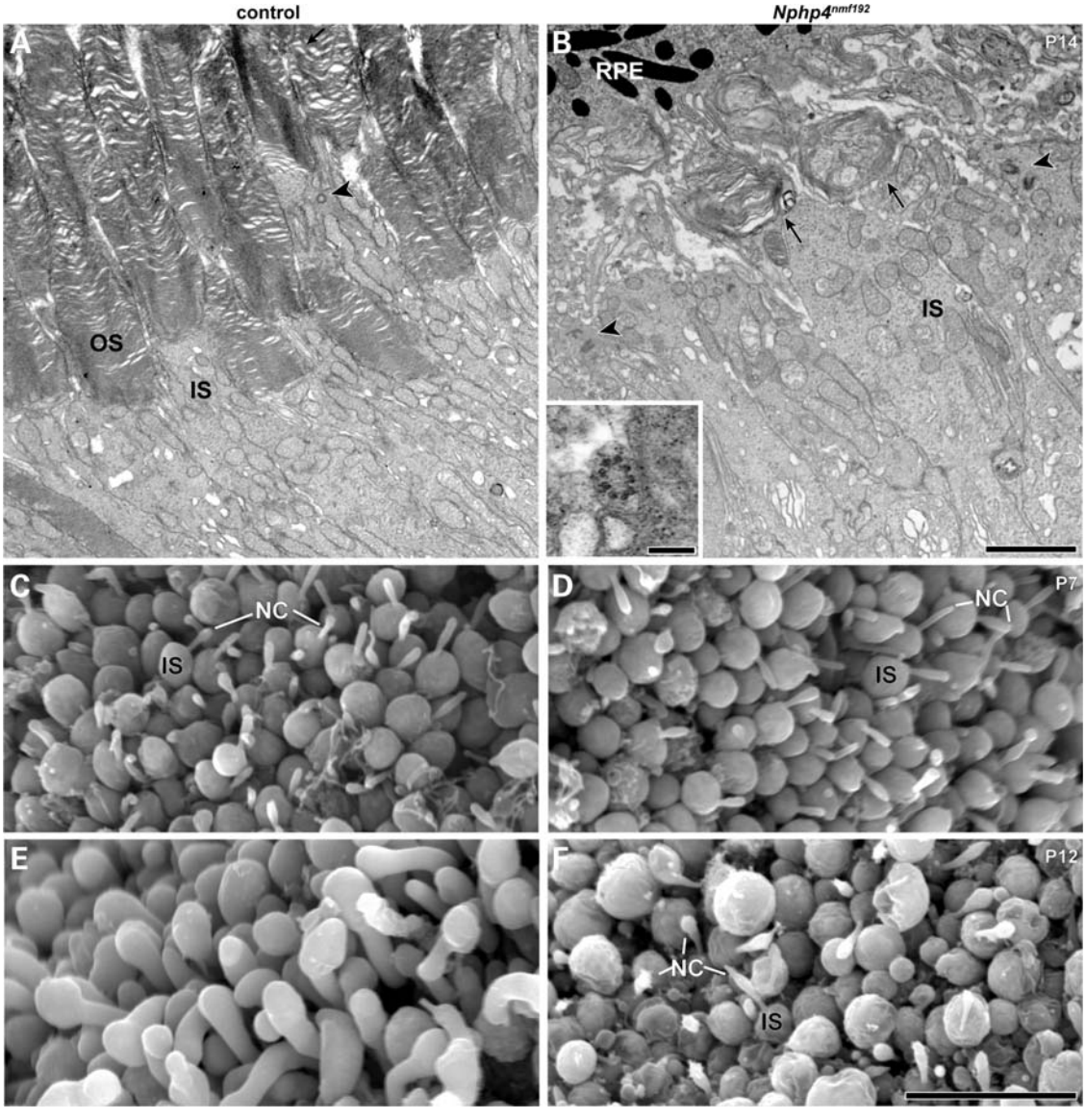

Figure 5. Ultrastructural analysis of the developing photoreceptor in mutant and WT mice. Rudimentary OS that failed to elongate were observed by transmission electron microscopy in mutant retinas at P14 (arrows, **A** and **B**). Basal bodies (arrow heads) were similar in structure in control and mutant retinas. A cross-section of mutant CC at P10 in insert of (B) shows the normal nine sets of doublets. Scanning electron microscopy revealed comparable CC number and length at P7 (**C** and **D**). But by P12, short and rudimentary OS were observed in mutant while well-organized and elongated paddle shape OS were found in littermate controls (**E** and **F**). NC, nascent cilia. Bars indicated 2 μm (A and B), 200 nm (insert of B) and 10 μm (C–F).

ONL of mutant mice as well. Like synaptophysin, little difference in post-synaptic denstity protein 95 (PSD95), a presynaptic marker in OPL, was discernable at P8 between mutants and controls (Supplementary Material, Fig. S5). However, by P12 the intensity of PSD95 staining of the OPL appeared to be greater for mutants than WT and by P14 a remarkable loss of PSD95 signal relative to controls was observed (Fig. 6C). Also, PSD95 staining appeared between photoreceptor nuclei at the innermost surface of the ONL. Western analysis was done to determine whether the difference in the intensity of PSD95 between P8 and P12 was due to a quantitative change. Because the total protein level of PSD95 was not different between control and mutant at P8 and P12 (Supplementary Material, Fig. S5), it suggests that the difference in IHC staining might reflect a change in the ribbon synapse structure. Interestingly, at P12, only a few peanut agglutinin (PNA) positive cone pedicles were detectable in the OPL of *Nphp4*$^{nmf192/nmf192}$ mutants compared with controls (Fig. 6D), perhaps contributing to the shortened OPL.

Anti-NPHP4 stained synaptic ribbons in the OPL, which could be blocked by pre-incubation with a recombinant N-terminal NPHP4 fragment (Fig. 6E), co-localized with RIBEYE, a synaptic ribbon protein, but not with Bassoon, a protein anchoring ribbons to the synaptic terminals (Fig. 6E). Some NPHP4 positive staining was also observed in PNA-positive cone pedicles in controls, indicating that NPHP4 is expressed in both rod and cone ribbons (Fig. 6E).

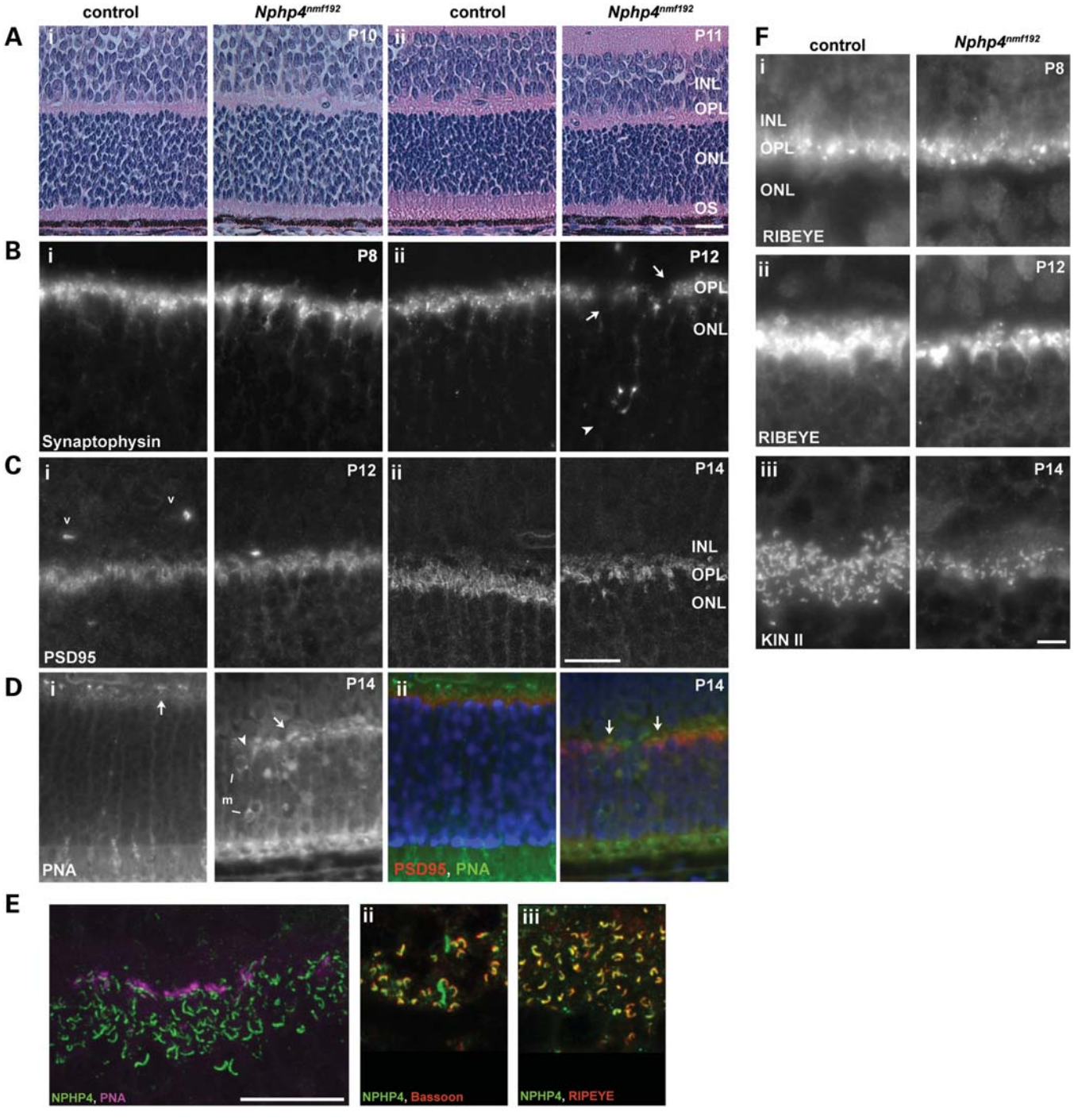

Figure 6. Synaptic ribbon defects in the OPL of *Nphp4*$^{nmf192/nmf192}$ mice. (**A**) The shortening of OPL was not obvious by light microscopy at P10 (i), whereas the shortening of OS was observable by P11 (ii). (**B**) Synaptophysin staining at P8 (i) and P12 (ii). Synaptophysin staining was discontinuous (arrows) and ectopic staining in the ONL (arrowhead) was observed at P12 (ii). (**C**) PSD95 was similar between mutant and controls at P12 (i) but reduced in staining intensity at P14 (ii). v indicates blood vessels stained with anti-mouse secondary antibodies. (**D**) Reduced PNA cone pedicle staining (arrows) and ectopic staining in ONL (arrowhead) were observed at P14 (i). Normally PSD95 and PNA do not colocalize at P14 (ii, left) but in the *Nphp4*$^{nmf192/nmf192}$ OPL some co-localization of these biomarkers were observed (arrows, ii), indicating the shortening of the OPL. m indicates the mislocalized PNA staining of the cone nucleus. (**E**) NPHP4 antibody stains rod and cone ribbons as indicated by double-staining with PNA (i), Bassoon (ii) and RIBEYE (iii). Arrows indicate cone pedicles stained with PNA. (**F**) Synaptic ribbons were stained with RIBEYE at P8 (i) and P12 (ii). OPL shortening was observed by staining with pre-synaptic marker kinesin-II (KIN) at P14 (iii). The typical horse-shoe shape of the ribbon synaptic terminal revealed by anti-kinesin-II staining was not well preserved in *Nphp4*$^{nmf192/nmf192}$ mutant retinas. Bars = 50 μm (A–D) and 20 μm (E and F).

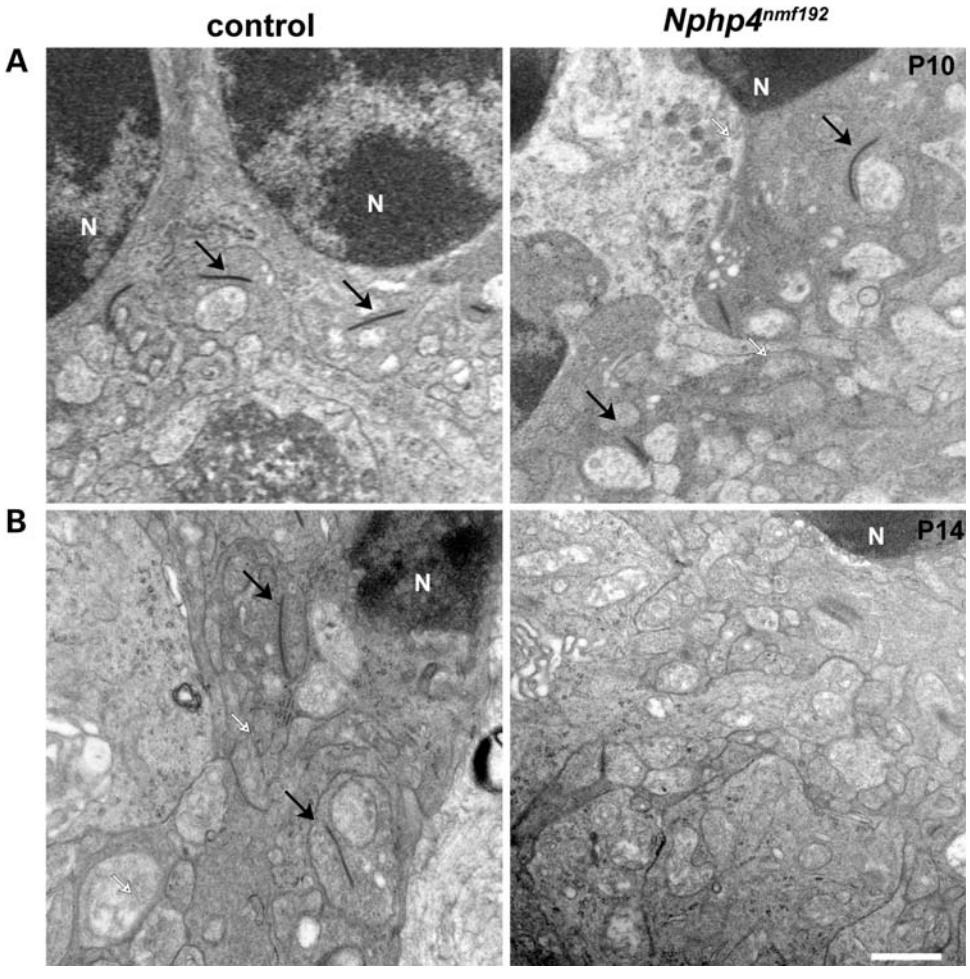

Figure 7. Ultrastructure of ribbon synapses is affected in *Nphp4*$^{nmf192/nmf192}$ mice. Developing ribbon synapses were examined by TEM at P10 (**A**) and P14 (**B**) in control and *Nphp4*$^{nmf192/nmf192}$ retinas. Ribbons are indicated by arrows, and N indicates the photoreceptor nucleus. Bar = 500 nm.

Synaptic ribbon biomarkers were examined in mutants and controls between P7 and P14, the time frame in which synaptic ribbons form (17,18). At P8, punctuate RIBEYE positive staining was found in the OPL in both mutants and controls at approximately the same intensities (Fig. 6F). However, by P12 the number of RIBEYE positive ribbons was reduced relative to controls and a qualitative difference in staining was observed. In WT, both punctuate and horseshoe-shaped staining patterns were observed, while in mutants, the majority of synaptic ribbons stained in a punctuate fashion. This difference was even more evident with kinesin II staining. In addition to a reduction in the number of synaptic ribbons at P14, mutant ribbons stained in punctuate or rod-like patterns with few, if any, horse-shoe shaped ribbons that were found in abundance in WT.

To determine whether the differences in synaptic ribbon staining were attributable to structural alterations in the ribbons themselves, we examined them by TEM at P8, P10 and P14 (Fig. 7). At P8, when cone synapses develop (18), ribbons were attached to the synaptic terminal, and synaptic vesicles were tethered around the synaptic ribbon in mutant and controls (data not shown). By P10, when rod synaptic ribbons develop (18), both the number and the length of synaptic ribbons increased in controls and *Nphp4*$^{nmf192/nmf192}$ mutants. The size and the structure of the synaptic ribbon in *Nphp4*$^{nmf192/nmf192}$ mutants were comparable with controls (Fig. 7). However, while we found two or three ribbons in each TEM field examined from controls, at P14, zero to one ribbon was observed in comparable fields from mutants (Fig. 6), confirming the reduction in RIBEYE and kinesin II staining observed in the OPL of *Nphp4*$^{nmf192/nmf192}$ mutants. The synaptic ribbons from mutants were short with ill-defined edges when compared with WT ribbons, which were elongated with slightly up-turned, tapered ends. Taken together, it appears that synaptic ribbons in *Nphp4*$^{nmf192/nmf192}$ mutants undergo normal early development in both cones and rods, and then rapidly degenerate by P14.

In addition to the deterioration of the ribbon synapse, abnormal horizontal cell processes were observed in the ONL of *Nphp4*$^{nmf192/nmf192}$ retinas at P11 (Supplementary Material, Fig. S5), prior to the loss of photoreceptor cell bodies. The abnormal processes were most prominent at P14. Remodeling of the synapses within the OPL has been observed previously in retinal degeneration models (19,20). However, these observations were made in mutant mice in which severe loss of photoreceptor cell bodies had already occurred. We, therefore,

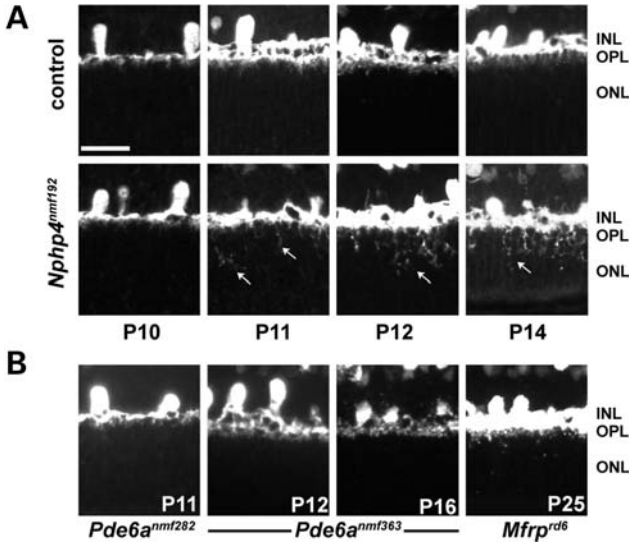

Figure 8. Ectopic horizontal cell processes are observed in *Nphp4*$^{nmf192/nmf192}$ mice. (**A**) The ectopic horizontal cell processes were observed as early as P11 in *Nphp4*$^{nmf192/nmf192}$ retina. Arrows indicate horizontal cell processes in the ONL. (**B**) Calbindin staining was observed in retinal sections from various photoreceptor degeneration models, which are not associated with cilia structure or function *per se*. Two *Pde6a* models, which show a very rapid degeneration, and *Mfrp*^{rd6} mutants, which show a relatively slow degeneration, were examined for ectopic horizontal cell processes. The tissues were collected at an early stage of degeneration when most of the cell bodies of the photoreceptor were retained in each animal model. None of the other models developed ectopic horizontal cell processes at the time points sampled. INL, inner nuclear layer; OPL, outer plexiform layer; ONL, outer nuclear layer. Bar = 50 μm.

sought to determine whether abnormal processes were also observed prior to significant loss of photoreceptor cell bodies in several different retinal degeneration models to determine whether the ectopic horizontal cell processes were simply a general phenomenon of all retinal degenerations (Fig. 8). We selected a number of models in which the molecular mechanism of retinal degeneration were not associated with the CC, and that demonstrated a range of disease onset and progression. Because the disease progression of these mouse models was different, we sampled at the age at which the majority of the ONL layer was intact, a period in which *Nphp4*$^{nmf192/nmf192}$ animals expressed the abnormal processes. Abnormal horizontal cell processes were not observed in mutants bearing alleles of *Pde6a* (21), an in-frame deletion of *Mfrp* (22), nor a new allele of *MerTK* (personal communication, data not shown). Therefore, the timing of the ectopic horizontal cell processes appears to be specific to the *Nphp4*$^{nmf192/nmf192}$ mutants and not a general phenomenon of mutants exhibiting a rapid loss of photoreceptor cells.

Reproductive function

Homozygous *Nphp4*$^{nmf192/nmf192}$ female mice were fertile with normal litter size and mating frequencies. In contrast, homozygous *Nphp4*$^{nmf192/nmf192}$ males failed to sire offspring (Table 1). Sperm was rarely found in the caudal epididymi in *Nphp4*$^{nmf192/nmf192}$ males and if found, displayed poor motility and failed to induce fertilization during *in vitro* fertilization (IVF) experiments (Table 1).

To determine whether mutant male mice show normal spermatogenesis, we examined both testicular and epididymal tissue histologically. Testes weight of *Nphp4*$^{nmf192/nmf192}$ mice did not differ from controls (Fig. 9A), ruling out testicular atrophy as the primary underlying cause of male infertility. Even at an advanced age, the mutant mice contained spermatogonial stem cells, as well as mature spermatozoa with elongated tails; however, the amount of spermatozoa in histological cross-sections of the testes in *Nphp4*$^{nmf192/nmf192}$ males was remarkably reduced compared with controls (Fig. 9G), and sperm counts from the caudal epidydimus confirmed a 98% reduction in mature spermatozoa in *Nphp4*$^{nmf192/nmf192}$ compared with controls (Fig. 9B). Few spermatozoa displayed movement (Fig. 9D), and those that did move had such poor quality of forward movement (Fig. 9E) that the sperm motility index (SMI) was insufficient to induce fertilization either *in vivo* or *in vitro* (Fig. 9C and Table 1). The impaired motility of sperm was not caused by disorganization of its flagellular axoneme as the cross-section and longitudinal electron microscope images of the flagella displayed an intact normal nine microtubule doublets encircling a central microtubule pair in both control and *Nphp4*$^{nmf192/nmf192}$ mutants (Fig. 9F). IHC results showed that NPHP4 localizes next to the basal bodies, stained by γ-tubulin in the testicular spermatozoa and spermatids (Fig. 9H). Epididymal spermatozoa and spermatozoa from the lumen of the testis were negative for both NPHP4 and γ-tubulin antibodies. NPHP4-positive staining was observed proximally, towards the sperm head relative to γ-tubulin. As with the photoreceptor synaptic ribbons, NPHP4 staining of the *Nphp4*$^{nmf192/nmf192}$ mutant testis was still observed at 6w (data not shown).

DISCUSSION

Although mutations within *NPHP4* are associated with NPHP and SLSD (5) in humans, the cellular functions of NPHP4 and the pathways leading to the observed pathologies are not well understood. Their similarities to other ciliopathies (1–3,23–26) suggest NPHP4 may participate in intraflagellar transport (IFT) or sensory signal transduction (27,28). A role for NPHP4 in cell adhesion and cytoskeleton modulation has also been indicated as NPHP4 has been found in cell–cell junctions with NPHP1 and actin-binding proteins (9).

The progress toward understanding the cellular role of NPHP4 has been hampered by the lack of an easily accessible animal model. While a deletion in *Nphp4* has been reported in a dog cone-rod dystrophy model (29), extensive studies have yet to be carried out. Here we report the first rodent model bearing a mutation in *Nphp4*. Contrary to our expectations, *Nphp4*$^{nmf192/nmf192}$ mice fail to develop the kidney abnormalities observed in humans. However, it should be noted that models bearing mutations in *Nphp1* and *Nphp6* also have normal kidney morphology and function (30,31), as does the cone-rod dystrophy dog model with an *Nphp4* mutation. While the protein sequence for NPHP4 is relatively conserved among human, mouse and dog, with 76–78% amino acid sequence identity, it is possible that the divergence of the remaining amino acids may lead to a structural or functional difference in NPHP4 in mouse and dogs. Alternatively, the

Table 1. Fertility in adult control and *Nphp4*$^{nmf192/nmf192}$ mutants

Genotype	Natural mating (%)	No. of litters per male	Timed mating (%)	Fertility (% sired)	Epididymal sperm (%)	IVF test (%)
Control	86	3	100	88	100	100
Nphp4$^{nmf192/nmf192}$	100	0	100	0*	13%*	0%*

Nphp4$^{nmf192/nmf192}$ males ($n = 8$) failed to sire offspring when mated to WT female mice. To determine whether male sterility was caused principally by a lack of coital behavior, male homozygous mutants were mated overnight with hormone-primed female WT mice. Copulatory plugs were found from all mutant ($n = 8$) and control ($n = 8$) male mice after mating. However, no pregnancies were detected in the mutant group, whereas nearly all WT males induced pregnancies. Sperm was found in the caudal epididymi in only one male *Nphp4*$^{nmf192/nmf192}$ mouse, while all control males contained motile sperm capable of inducing fertilization and producing embryos during IVF experiments. The sperm from the one male mutant with caudal epididymal sperm, displayed poor motility and failed to induce fertilization during IVF experiments.

*$P < 0.01$.

χ^2 tests.

dissimilarity in kidney pathology of the animal models and type 4 NPHP patients may be explained by species variation in tissue expression profiles, availability of compensatory molecules in mouse and dog, and/or physiological differences of organs between species. It is also possible that the B6 genetic background confers protection against kidney dysfunction in *Nphp4*$^{nmf192/nmf192}$ mice. *Tmem67*^{bpck} mice show a less severe kidney phenotype in a mixed background than in either B6 or C3H/HeJ congenic lines (32).

Ciliopathies, such as primary cilia dyskinesia (PCD), are often associated with infertility (23). Contrary to our expectations, however, the male infertility in *Nphp4*$^{nmf192/nmf192}$ mice does not appear to be caused by an underlying disorganization of the axoneme in the flagella of the spermatozoa, as the nine doublet and central pairs of microtubules are ultrastructurally intact as revealed by our electron microscopy data. Also, a lack of circulating testosterone is unlikely to contribute to the infertility because mating behavior is intact and the gonads are of normal size. Nevertheless, it is clear from our experiments that insufficient sperm motility, coupled with a 98% loss of spermatozoa, underlies the infertility in male *Nphp4*$^{nmf192/nmf192}$ mice.

While the *Nphp4*^{nmf192} mouse model does not fully recapitulate human type 4 NPHP, it does develop the retinal disease observed in patients with SLSD, which has been reported to range from Leber congenital amaurosis (LCA) to RP (2). The early and rapid loss of photoreceptors and visual function observed in *Nphp4*$^{nmf192/nmf192}$ mutants is most reminiscent of LCA and may be attributed in part to the defects in OS development. Fully elongated OS with mature discs observed in WT mice were never detected in *Nphp4*$^{nmf192/nmf192}$ mutants. Instead, short and disorganized OS remnants were seen at the ultrastructural level. As a ciliopathy, the abnormal OS development could be explained by defects in the CC, a modified cilia structure. Recently, NPHP4 has been proposed to regulate localization of the IFT machinery and of axonemal components (33). Morphologically, however, as with other ciliopathies (34,35), the CC appears to be intact in *Nphp4*$^{nmf192/nmf192}$ mutants. While transport of molecules such as rod transducin and arrestin did not appear to be affected at P14, transport of rhodopsin, a molecule necessary for OS elongation and elaboration, is affected by the loss of NPHP4 function.

The disease features of *Nphp4*$^{nmf192/nmf192}$ eyes are very similar phenotypically to that of *Rpgrip1*^{nmf247} mutants, a null allele of *Rpgrip1* (15). Like NPHP4, mutations in RPGRIP1 are associated with LCA, and the mouse models of *Rpgrip1* exhibit early retinal degeneration (15,36). Both *Nphp4*$^{nmf192/nmf192}$ and *Rpgrip1*$^{nmf247/nmf247}$ mutants show a similar rapid rate of photoreceptor degeneration with only one layer of nuclei left in the ONL by 4w. RPGRIP1, which also localizes to the CC in mouse, has been shown to directly interact with NPHP4 in both *in vivo* and *in vitro* assays (6). Our data suggest that NPHP4 may assist in the localization of RPGRIP1 to the CC, in a similar manner, as RPGRIP1 is necessary for the tethering of RPGR to the CC (36). RPGRIP1 and NPHP4, however, are likely to play non-complimentary, non-redundant roles within the retina as compound heterozygous *Nphp4*$^{nmf192/+}$, *Rpgrip1*$^{nmf247/+}$ mice have normal retinas (data not shown).

An interesting finding in the retina of *Nphp4*$^{nmf192/nmf192}$ mutants was the abnormal OPL, where photoreceptors synapse with secondary neurons. Previous studies have shown NPHP4 localization to the OPL (6,37). Our investigations suggest that NPHP4 localizes to the synaptic ribbons in the OPL. The synaptic ribbons, however, appear to develop normally in mutant mice until P8 as the localization and intensities of synaptic markers, and ultrastructure were similar to controls. However, by P14, a rapid deterioration of the ribbons was observed by ultrastructural studies with abnormal patterns of staining of ribbon markers. Our observations suggest that if NPHP4 has a direct function in the synapse, then it does not appear to be necessary for the early assembly of the synaptic ribbon, but may be necessary for its maintenance.

Abnormal synapses have also been reported for knock-out (KO) models of synaptic ribbon components such as *Bassoon* and *Kif3a*; voltage-gated channel components such as *CaBP4* and *Cacna1f*; and cytoskeleton related proteins such as *Myosin Va* and *Laminin ß2* (38–43). However, in each case while some of the abnormalities reported were similar to that observed in *Nphp4*^{nmf192} mutants, many were not. For example, *Laminin ß2* deficient mice exhibit an increased number of floating ribbons, while most of the synaptic ribbons float in *Bassoon* KO mice (38,40); a phenotype not observed in *Nphp4*$^{nmf192/nmf192}$ mutants. ERG b-wave is absent in *Cacna1f* mutant mice (*nob2*) under light- and dark-adapted conditions, and ectopic horizontal processes and abnormal staining with synaptic markers are observed in *Cacna1f* ^{nob2} retina (43). Likewise, *CaBP4* KO mice show punctuate staining of ribbon markers with ectopic horizontal and bipolar processes (42). Finally, while photoreceptor ribbons are

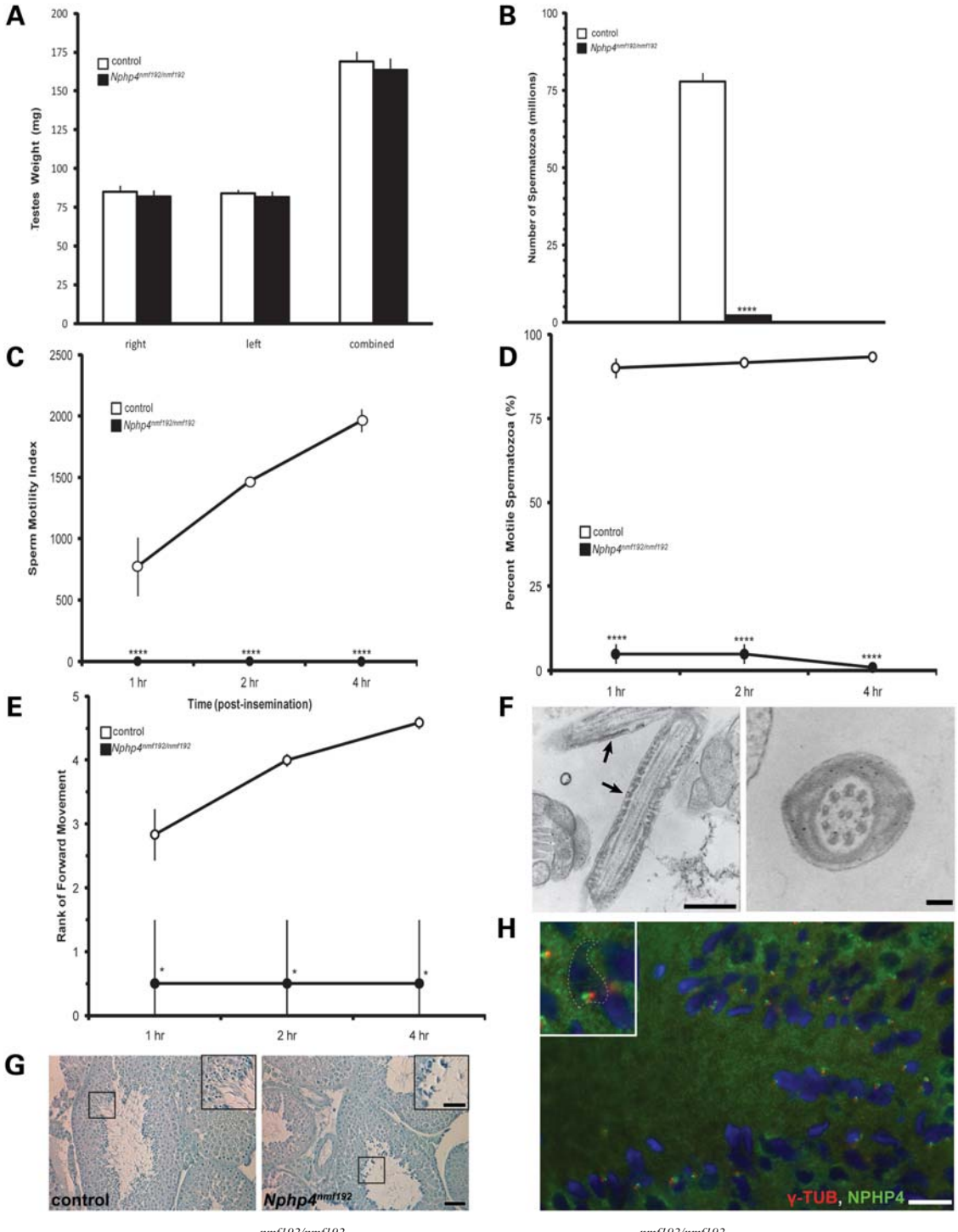

Figure 9. Male infertility was observed in *Nphp4*$^{nmf192/nmf192}$ mice. Testes size was normal in *Nphp4*$^{nmf192/nmf192}$ compared with control (**A**), however spermatozoa counts (**B**) and amount of motile sperm (**D**) were extremely low, with little forward movement (**E**, $^{*}P < 0.01$), and SMI necessary for fertilization was nonexistent (**C**, $^{****}P < 0.0001$). TEM revealed that *Nphp4*$^{nmf192/nmf192}$ spermatozoa had intact axoneme in both longitudinal (**F**, left panel) and cross-sections, with 9+2 flagella structure in sperm tails (F, right panel). Normal early spermatogenesis, albeit few fully mature spermatozoa (insets), was observed in *Nphp4*$^{nmf192/nmf192}$ compared with control testis by toluene blue staining (**G**). (**H**) NPHP4 did not colocalize with γ-tubulin, the centriole marker in testicular sperm. Insert is a ×2 magnified image and sperm head is visualized with a dashed line. Bars = 50 μm (G), 25 μm (insets in G), 500 nm (F, left panel), 100 nm (F right panel) and 10 μm (H).

morphologically compromised in *MyoVa* deficient mice (39), their localization is normal. Ectopic horizontal cell processes with synapses within the OPL and ectopic cone pedicles in the ONL are present in the retina of *Nphp4*$^{nmf192/nmf192}$ mice as early as P11. However, unlike *Bassoon* and *Cacna1f* mutant mice, ectopic bipolar dendrites were not observed in

Nphp4$^{nmf192/nmf192}$ mutants. A conditional KO model of *Kif3a*, a molecular motor protein for vesicle transport across the CC and a ribbon component exhibit both photoreceptor nuclei loss and OPL defects (40). Like KIF3A, it is possible that NPHP4, which localizes to both the ribbons and CC, plays a necessary and similar functional role at both sites.

In summary, we describe disease phenotypes of *Nphp4*$^{nmf192/nmf192}$ mutant mice generated by ENU chemical mutagenesis. Analyses of mutant mice show defective OS and synaptic ribbon morphogenesis and ectopic horizontal cell dendrites in the retina, and male infertility. This *Nphp4*^{nmf192} mouse model will be useful for dissecting the roles of NPHP4 in the retina and spermatogenesis, and for providing a resource to elucidate the mechanisms underlying the molecular pathogenesis observed.

MATERIALS AND METHODS

Origin of mutant mice and husbandry

Homozygous *nmf192* mice were identified in a B6 G3 ENU mutagenesis screen (http://nmf.jax.org). Mice, bred and housed in the Research Animal Facility, were provided NIH31 6% fat diet, and acidified water in a vivarium with a 12-h light/12-h dark cycle. All experimental procedures were approved by The Jackson Laboratory Animal Care and Use Committee. For dark rearing, mice were bred and maintained in a dark room under the same housing conditions. Filtered red light was used to carry out the maintenance of the mice and to collect samples.

For examining the stimulus-dependent translocation of signaling molecules in the retina, a group of mice were dark adapted for 16 h. Alternatively, for light stimulus, mice were treated with 1% atropine eye drops and transferred to a mirrored box in which they were exposed to 1300 lux of light for 30 min. Eyes enucleated from mice euthanized by carbon dioxide asphyxiation were processed as described below.

For examining light-induced degeneration, mice were dark-adapted overnight. Prior to bright light exposure, pupils were dilated with atropine. The mice were exposed to 12 000 lux of light for 1 h in a mirrored box and returned to normal 12-h light/12-h dark cycle vivarium conditions. Eyes were collected for histology 14 days after bright light exposure.

Visual and auditory examination

For the ophthalmic examination, pupils were dilated with atropine prior to examination by indirect ophthalmoscopy using a 60 diopter aspheric lens. Detailed methods and equipment used for fundus photography and ERG have been previously described (34).

For the hearing function, mice were assessed by ABR threshold analysis. The ABR threshold was recorded in dB SPL (decibels, sound pressure level) for click, 8 kHz, 16 kHz and 32 kHz sound. Detailed methods have been previously described (44).

Genetic mapping and sequence analysis

For chromosomal localization of the mutation, affected *nmf192*/*nmf192* females maintained on a B6 genetic background were outcrossed with male DBA/2J mice. The resulting F1 progeny was intercrossed to generate F2 offspring, which were phenotyped by indirect ophthalmoscopy. Genomic DNA was isolated from tail tips using a PCR Buffer with Nonionic Detergents (PBND) preparation (15) or a simple salt precipitation method (45). A DNA pooling strategy described by Taylor and Phillips (46) was carried out in which genomic DNA from 10 affected and 10 unaffected mice were pooled separately and screened in a genome-wide scan using 92 SSLP markers. Three hundred forty-four DNAs isolated from F2 offspring were tested for recombinations with *D4Mit42* and *D4Mit344*, markers flanking the critical region. DNA from 51 F2 mice that were recombinant within the region was tested individually for fine mapping of the chromosomal region.

For the light sensitivity modifier test, affected female B6-*Nphp4*$^{nmf192/nmf192}$ mice were outcrossed to 129 male mice. The resulting B6;129 *Nphp4*$^{+/nmf192}$ F1 mice and both parental strains were used for the light-stimulated degeneration study, as describe above.

For coding sequence comparisons, total RNA was isolated from whole eyes of affected animals, B6 control, 129 and BALB/cJ using TRizol Reagent (Life Technologies). The evaluation of the RNA quality, method for cDNA preparation and PCR protocols were described previously (15). Ten primer sets (Supplementary Material, Table S2) were used for amplifying the entire coding region of *Nphp4* and PCR amplicons were sequenced on an Applied Biosystems 3730XL sequencer.

Histological and IHC analyses

The protocols for histology and immunohistochemistry were described previously (34). Briefly, the enucleated eyes were fixed overnight in cold methanol/acetic acid solution (3:1, v/v), embedded in paraffin and cut into 6 μm sections for hematoxylin and eosin (H&E) staining or IHC analysis. Alternatively, fresh eyes or testis were frozen in optical cutting temperature (Tissue-Tek) compound, and cut into 10 μm section, followed by cold acetone fixation prior to IHC analysis. Occasionally, dissected retinas were fixed 2 h in cold 4% paraformaldehyde (PFA) and incubated overnight in 30% sucrose solution. The fixed retinas were frozen and cut in the same manner as fresh tissue described above without acetone fixation.

The protocol for quantification of ONLT was previously described (47,48). ONL and INL thicknesses were measured in a single 5 μm section stained by H&E. Three measurements were made at each nine, 0.25 mm interval in both superior and inferior hemispheres using ImageJ software. ONLT index, which is the ONLT normalized by the corresponding INL thickness, was assessed at P19, when the INL was comparable with controls, to correct for artificial variability such as oblique sectioning (47). Sections with the widest area of optic nerve head and uniform alignment of both ONL and INL with well-focused IS throughout entire section were selected for quantification.

Polyclonal NPHP4 antibody was raised against a HIS-fusion N-terminal NPHP4 fragment (188 amino acids). For competitive antigen blocking studies, 1 μg/ml of immunizing protein was pre-incubated with anti-NPHP4 prior to use on sections.

For IHC studies, sections were incubated with anti-rhodopsin (1:500; Leico Technologies), anti-ROM-1 (1:500; a kind gift from R. Mclnnes), anti-calbindin (1:300; Abcam), anti-ribeye (1:300; BD), anti-post-synaptic density protein 95 (PSD95, 1:200; Upstate), anti-kinesin II (1:200; Covance), anti-protein kinase C alpha (1:200; Abcam), anti-α transducing activity polypeptide 1 (GNAT1, 1:200; Santa Cruz), anti-arrestin (1:500; ABR), anti-acetylated tubulin (1:250; Sigma), anti-caspase-3 (1:100; Cell Signaling), anti-IFT88 (1:1000, a kind gift from B. Yoder), anti-RPGR (1:1000, 49) and anti-RPGRIP1 (1:200; 36). Localization of specific proteins was visualized by fluorescence microscopy or confocal microscopy following Cy-3 conjugated secondary antibody (1:200; Jackson Immunoresearch) labeling. For whole-mount staining, enucleated eyes were immersion fixed in 4% PFA for 5 min. Retinas were dissected and stained with anti-red/green opsin (1:200; Chemicon) in a cold chamber with agitation for 2 days, and followed by an overnight incubation with Cy-3 conjugated secondary antibody. Sections were examined by confocal microscopy.

Western analysis

Total protein from whole eyes was isolated using lysate buffer (1% NP-40, 0.1% SDS and 0.5 % sodium deoxycholate in PBS). One hundred micrograms of total protein were electrophoretically separated on a 10% SDS–polyacrylamide gel and transferred onto a nitrocellulose membrane. The membrane was stained with antibodies and visualized using the ECL detection system (Perkin-Elmer).

Reproductive physiology

To assess fertility, spontaneous mating experiments were conducted for 12 weeks using both adult male and female homozygous mutants and WT mice ($n = 8$/genotype and sex). Age-matched, homozygous mutant and WT mice were mated to either 6-week-old female or 12-week-old male B6 mice and the number of litters was recorded. In another group of mice, timed-mating experiments were conducted to detect behavioral abnormalities associated with infertility. For these experiments, adult female B6 mice were primed with pregnant mare serum gonadotropin (5 IU, ip, Sigma) followed 44–46 h later by administration of human chorionic gonadotropin (5 UI, ip, Sigma) to induce ovulation, and were mated overnight with either adult homozygous mutants or WT male mice ($n = 8$ per genotype). Hormone-primed females were assessed for coitus by the presence of a copulatory plug the following morning, and for pregnancy by palpitation. The percentage of male mice that successfully mated and sired offspring were recorded and analyzed statistically using χ^2-tests to detect significant differences.

Sperm motility, countsand *in vitro* fertilization

In mice, spermatogenesis yields fully formed spermatozoa in the testes that enter the caput epididymis in an immature state, not capable of motility and fertilization. Spermatozoa complete their maturation while transitioning via peristalsis from caput to caudal epididymis, which absorbs testicular fluid to concentrate the sperm. Full capacitation of spermatozoa occurs outside the male reproductive tract and only fully capacitated sperm can induce fertilization. Sperm count and motility tests were conducted in accordance with capacitation by releasing sperm from the caudal epididymis into the petri dish with IVF culture media. Sperm motility was evaluated in duplicate for each mouse on at least 100 sperm to assess the percentage of motile sperm and quality of forward progressive movement (fpm) at 1, 2 and 4 h after release from the caudal epididymis. The quality of fpm was evaluated by a standard scale (50,51). A SMI was calculated for each replicate at each time interval (SMI = fpm score X % motile cells) (50,51). Sperm were counted in duplicate for each mouse using a hemocytometer, magnified ×50. Additional sperm samples were diluted in fixative (1:2), centrifuged (5000 rpm for 30 s) to concentrate sperm and processed for TEM, as previously described (15).

For IVF tests, caudal epididymal sperm, from adult 10- to 14-week-old homozygous mutant and WT males, were harvested to inseminate 40–60 ovulated oocytes (B6 female mice) collected per donor male and cultured for 4 h at 37°C in miniature CO_2 incubators (New Brunswick Scientific, NJ, USA). Fertilization was carried out for 4 h in minimum essential medium prepared with Earle's balanced salt solution, containing both essential and non-essential amino acids (Gibco) 0.23 mM pyruvic acid, 75 mg/l penicillin G, 50 mg/l streptomycin sulfate, 0.01 mM tetra sodium EDTA (Sigma) and 3 mg/ml BSA (Sigma). After fertilization, all oocytes were collected, washed twice in fresh medium and cultured overnight in 1 ml of the same medium. Embryos that cleaved to the two-cell stage were counted, collected and washed twice in KSO medium supplemented with essential and non-essential amino acids and permitted to develop until the blastocyst stage in this medium (52,53).

Gonadal histology

Adult homozygous mutant and WT male mice were killed by cervical dislocation, and immediately perfused with 2 ml of physiological saline (pH 7.4, 4°C). Testes were collected and immersed overnight in Bouin's fixative. Tissues were rinsed three times, paraffin-embedded and sectioned at 5 μm on a microtome. To assess the presence of spermatozoa, separate slides were processed using the cytological stains, Periodic acid-Schiff and toluene blue. Images were collected with a digital camera attached to a Leica DMRB microscope, under ×20 objective.

SUPPLEMENTARY MATERIAL

Supplementary Material is available at *HMG* online.

ACKNOWLEDGEMENTS

We thank Drs Kenneth Johnson and Doyeun Kim for careful review for this manuscript. We also thank Douglas Howell for ERG testing of rod and cone function.

Conflict of Interest statement. None declared.

FUNDING

This study was supported by National Institutes of Health grants (EY016501 to P.M.N., AA017244 to C.M.); a TJL institutional core grant (CA34196) and the Foundation for Fighting Blindness.

REFERENCES

1. Hildebrandt, F. and Otto, E. (2000) Molecular genetics of nephronophthisis and medullary cystic kidney disease. *J. Am. Soc. Nephrol.*, **11**, 1753–1761.
2. Saunier, S., Salomon, R. and Antignac, C. (2005) Nephronophthisis. *Curr. Opin. Genet. Dev.*, **15**, 324–331.
3. Krishnan, R., Eley, L. and Sayer, J.A. (2008) Urinary concentration defects and mechanisms underlying nephronophthisis. *Kidney Blood Press Res.*, **31**, 152–162.
4. Hildebrandt, F. and Omram, H. (2001) New insights: nephronophthisis-medullary cystic kidney disease. *Pediatr. Nephrol.*, **16**, 168–176.
5. Mollet, G., Salomon, R., Gribouval, O., Silbermann, F., Bacq, D., Landthaler, G., Milford, D., Nayir, A., Rizzoni, G., Antignac, C. *et al.* (2002) The gene mutated in juvenile nephronophthisis type 4 encodes a novel protein that interacts with nephrocystin. *Nat. Genet.*, **32**, 300–305.
6. Roepman, R., Letteboer, S.J., Arts, H.H., van Beersum, S.E., Lu, X., Krieger, E., Ferreira, P.A. and Cremers, F.P. (2005) Interaction of nephrocystin-4 and RPGRIP1 is disrupted by nephronophthisis or Leber congenital amaurosis-associated mutations. *Proc. Natl Acad. Sci. USA*, **102**, 18520–18525.
7. Delous, M., Baala, L., Salomon, R., Laclef, C., Vierkotten, J., Tory, K., Golzio, C., Lacoste, T., Besse, L., Ozilou, C. *et al.* (2007) The ciliary gene *RPGRIP*1L is mutated in cerebello-oculo-renal syndrome (Joubert syndrome type B) and Meckel syndrome. *Nat. Genet.*, **39**, 875–881.
8. Murga-Zamalloa, C.A., Desai, N.J., Hildebrandt, F. and Khanna, H. (2010) Interaction of ciliary disease protein retinitis pigmentosa GTPase regulator with nephronophthisis-associated proteins in mammalian retinas. *Mol. Vis.*, **16**, 1373–1381.
9. Mollet, G., Silbermann, F., Delous, M., Salomon, R., Antignac, C. and Saunier, S. (2005) Characterization of the nephrocystin/nephrocystin-4 complex and subcellular localization of nephrocystin-4 to primary cilia and centrosomes. *Hum. Mol. Genet.*, **14**, 645–656.
10. Otto, E., Hoefele, J., Ruf, R., Mueller, A.M., Hiller, K.S., Wolf, M.T., Schuermann, M.J., Becker, A., Birkenhäger, R., Sudbrak, R. *et al.* (2002) A gene mutated in nephronophthisis and retinitis pigmentosa encodes a novel protein, nephroretinin, conserved in evolution. *Am. J. Hum. Genet.*, **71**, 1161–1167.
11. May-Simera, H.L., Ross, A., Rix, S., Forge, A., Beales, P.L. and Jagger, D.J. (2009) Patterns of expression of Bardet-Biedl syndrome proteins in the mammalian cochlea suggest noncentrosomal functions. *J. Comp. Neurol.*, **514**, 174–188.
12. Liu, X.Z., Walsh, J., Mburu, P., Kendrick-Jones, J., Cope, M.J., Steel, K.P. and Brown, S.D. (1997) Mutations in the *myosin VIIA* gene cause non-syndromic recessive deafness. *Nat. Genet.*, **16**, 188–190.
13. Walton, J.P., Barsz, K. and Wilson, W.W. (2008) Sensorineural hearing loss and neural correlates of temporal acuity in the inferior colliculus of the C57BL/6 mouse. *J. Assoc. Res. Otolaryngol.*, **9**, 90–101.
14. Danciger, M., Lyon, J., Worrill, D., Hoffman, S., Lem, J., Reme, C.E., Wenzel, A. and Grimm, C. (2004) New retinal light damage QTL in mice with the light-sensitive RPE65 LEU variant. *Mamm. Genome*, **15**, 277–283.
15. Won, J., Gifford, E., Smith, R.S., Yi, H., Ferreira, P.A., Hicks, W.L., Li, T., Naggert, J.K. and Nishina, P.M. (2009) RPGRIP1 is essential for normal rod photoreceptor outer segment elaboration and morphogenesis. *Hum. Mol. Genet.*, **18**, 4329–4339.
16. Morrow, E.M., Furukawa, T., Raviola, E. and Cepko, C.L. (2005) Synaptogenesis and outer segment formation are perturbed in the neural retina of *Crx* mutant mice. *BMC Neurosci.*, **6**, 5.
17. tom Dieck, S. and Brandstätter, J.H. (2006) Ribbon synapses of the retina. *Cell Tissue Res.*, **326**, 339–346.
18. Regus-Leidig, H., tom Dieck, S., Specht, D., Meyer, L. and Brandstätter, J.H. (2009) Early steps in the assembly of photoreceptor ribbon synapses in the mouse retina: the involvement of precursor spheres. *J. Comp. Neurol.*, **512**, 814–824.
19. Marc, R.E., Jones, B.W., Anderson, J.R., Kinard, K., Marshak, D.W., Wilson, J.H., Wensel, T. and Lucas, R.J. (2007) Neural reprogramming in retinal degeneration. *Invest. Ophthalmol. Vis. Sci.*, **48**, 3364–3371.
20. Jones, B.W., Watt, C.B., Frederick, J.M., Baehr, W., Chen, C.K., Levine, E.M., Milam, A.H., Lavail, M.M. and Marc, R.E. (2003) Retinal remodeling triggered by photoreceptor degenerations. *J. Comp. Neurol.*, **464**, 1–16.
21. Sakamoto, K., McCluskey, M., Wensel, T.G., Naggert, J.K. and Nishina, P.M. (2009) New mouse models for recessive retinitis pigmentosa caused by mutations in the *Pde6a* gene. *Hum. Mol. Genet.*, **18**, 178–192.
22. Won, J., Smith, R.S., Peachey, N.S., Wu, J., Hicks, W.L., Naggert, J.K. and Nishina, P.M. (2008) Membrane frizzled-related protein is necessary for the normal development and maintenance of photoreceptor outer segments. *Vis. Neurosci.*, **25**, 563–574.
23. Bisgrove, B.W. and Yost, H.J. (2006) The roles of cilia in developmental disorders and disease. *Development*, **133**, 4131–4143.
24. Katsanis, N., Beales, P.L., Woods, M.O., Lewis, R.A., Green, J.S., Parfrey, P.S., Ansley, S.J., Davidson, W.S. and Lupski, J.R. (2000) Mutations in *M*KKS cause obesity, retinal dystrophy and renal malformations associated with Bardet-Biedl syndrome. *Nat. Genet.*, **26**, 67–70.
25. Collin, G.B., Marshall, J.D., Ikeda, A., So, W.V., Russell-Eggitt, I., Maffei, P., Beck, S., Boerkoel, C.F., Sicolo, N., Martin, M. *et al.* (2002) Mutations in *AL*MS1 cause obesity, type 2 diabetes and neurosensory degeneration in Alström syndrome. *Nat. Genet.*, **31**, 74–78.
26. Nauli, S.M., Alenghat, F.J., Luo, Y., Williams, E., Vassilev, P., Li, X., Elia, A.E., Lu, W., Brown, E.M., Quinn, S.J. *et al.* (2003) Polycystins 1 and 2 mediate mechanosensation in the primary cilium of kidney cells. *Nat. Genet.*, **33**, 129–137.
27. Jauregui, A.R. and Barr, M.M. (2005) Functional characterization of the C. elegans nephrocystins NPHP-1 and NPHP-4 and their role in cilia and male sensory behaviors. *Exp. Cell Res.*, **305**, 333–342.
28. Wolf, M.T., Lee, J., Panther, F., Otto, E.A., Guan, K.L. and Hildebrandt, F. (2005) Expression and phenotype analysis of the nephrocystin-1 and nephrocystin-4 homologs in Caenorhabditis elegans. *J. Am. Soc. Nephrol.*, **16**, 676–687.
29. Wiik, A.C., Wade, C., Biagi, T., Ropstad, E.O., Bjerkås, E., Lindblad-Toh, K. and Lingaas, F. (2008) A deletion in nephronophthisis 4 (*NP*HP4) is associated with recessive cone-rod dystrophy in standard wire-haired dachshund. *Genome Res.*, **18**, 1415–1421.
30. Jiang, S.T., Chiou, Y.Y., Wang, E., Lin, H.K., Lee, S.P., Lu, H.Y., Wang, C.K., Tang, M.J. and Li, H. (2008) Targeted disruption of *Nphp1* causes male infertility due to defects in the later steps of sperm morphogenesis in mice. *Hum. Mol. Genet.*, **17**, 3368–3379.
31. Chang, B., Khanna, H., Hawes, N., Jimeno, D., He, S., Lillo, C., Parapuram, S.K., Cheng, H., Scott, A., Hurd, R.E. *et al.* (2006) In-frame deletion in a novel centrosomal/ciliary protein CEP290/NPHP6 perturbs its interaction with RPGR and results in early-onset retinal degeneration in the *rd16* mouse. *Hum. Mol. Genet.*, **15**, 1847–1857.
32. Cook, S.A., Collin, G.B., Bronson, R.T., Naggert, J.K., Liu, D.P., Akeson, E.C. and Davisson, M.T. (2009) A mouse model for Meckel syndrome type 3. *J. Am. Soc. Nephrol.*, **20**, 753–764.
33. Jauregui, A.R., Nguyen, K.C., Hall, D.H. and Barr, M.M. (2008) The Caenorhabditis elegans nephrocystins act as global modifiers of cilium structure. *J. Cell Biol.*, **180**, 973–988.
34. Collin, G.B., Cyr, E., Bronson, R., Marshall, J.D., Gifford, E.J., Hicks, W., Murray, S.A., Zheng, Q.Y., Smith, R.S., Nishina, P.M. *et al.* (2005) *Alms1*-disrupted mice recapitulate human Alström syndrome. *Hum. Mol. Genet.*, **14**, 2323–2333.
35. Davis, R.E., Swiderski, R.E., Rahmouni, K., Nishimura, D.Y., Mullins, R.F., Agassandian, K., Philp, A.R., Searby, C.C., Andrews, M.P., Thompson, S. *et al.* (2007) A knockin mouse model of the Bardet-Biedl syndrome 1 M390R mutation has cilia defects, ventriculomegaly, retinopathy, and obesity. *Proc. Natl Acad. Sci. USA*, **104**, 19422–19427.
36. Zhao, Y., Hong, D.H., Pawlyk, B., Yue, G., Adamian, M., Grynberg, M., Godzik, A. and Li, T. (2003) The retinitis pigmentosa GTPase regulator (RPGR)-interacting protein: subserving RPGR function and participating in disk morphogenesis. *Proc. Natl Acad. Sci. USA*, **100**, 3965–3970.
37. Arts, H.H., Doherty, D., van Beersum, S.E., Parisi, M.A., Letteboer, S.J., Gorden, N.T., Peters, T.A., Märker, T., Voesenek, K., Kartono, A. *et al.* (2007) Mutations in the gene encoding the basal body protein RPGRIP1L,

a nephrocystin-4 interactor, cause Joubert syndrome. *Nat. Genet.*, **39**, 882–888.
38. Libby, R.T., Lavallee, C.R., Balkema, G.W., Brunken, W.J. and Hunter, D.D. (1999) Disruption of laminin beta2 chain production causes alterations in morphology and function in the CNS. *J. Neurosci.*, **19**, 9399–9411.
39. Libby, R.T., Lillo, C., Kitamoto, J., Williams, D.S. and Steel, K.P. (2004) Myosin Va is required for normal photoreceptor synaptic activity. *J. Cell Sci.*, **117**, 4509–4515.
40. Muresan, V., Lyass, A. and Schnapp, B.J. (1999) The kinesin motor KIF3A is a component of the presynaptic ribbon in vertebrate photoreceptors. *J. Neurosci.*, **19**, 1027–1037.
41. Dick, O., tom Dieck, S., Altrock, W.D., Ammermüller, J., Weiler, R., Garner, C.C., Gundelfinger, E.D. and Brandstätter, J.H. (2003) The presynaptic active zone protein bassoon is essential for photoreceptor ribbon synapse formation in the retina. *Neuron*, **37**, 775–786.
42. Haeseleer, F., Imanishi, Y., Maeda, T., Possin, D.E., Maeda, A., Lee, A., Rieke, F. and Palczewski, K. (2004) Essential role of Ca2+-binding protein 4, a Cav1.4 channel regulator, in photoreceptor synaptic function. *Nat. Neurosci.*, **7**, 1079–1087.
43. Chang, B., Heckenlively, J.R., Bayley, P.R., Brecha, N.C., Davisson, M.T., Hawes, N.L., Hirano, A.A., Hurd, R.E., Ikeda, A., Johnson, B.A. *et al.* (2006) The *nob2* mouse, a null mutation in *Cacna1f*: anatomical and functional abnormalities in the outer retina and their consequences on ganglion cell visual responses. *Vis. Neurosci.*, **23**, 11–24.
44. Johnson, K.R., Longo-Guess, C., Gagnon, L.H., Yu, H. and Zheng, Q.Y. (2008) A locus on distal chromosome 11 (*ahl8*) and its interaction with *Cdh23 ahl* underlie the early onset, age-related hearing loss of DBA/2J mice. *Genomics*, **92**, 219–225.
45. Miller, S.A., Dykes, D.D. and Polesky, H.F. (1988) A simple salting out procedure for extracting DNA from human nucleated cells. *Nucleic Acids Res.*, **16**, 1215.
46. Taylor, B.A. and Phillips, S.J. (1996) Detection of obesity QTLs on mouse chromosomes 1 and 7 by selective DNA pooling. *Genomics*, **34**, 389–398.
47. Ikeda, A., Naggert, J.K. and Nishina, P.M. (2002) Genetic modification of retinal degeneration in tubby mice. *Exp. Eye Res.*, **74**, 455–461.
48. LaVail, M.M., Gorrin, G.M., Repaci, M.A., Thomas, L.A. and Ginsberg, H.M. (1987) Genetic regulation of light damage to photoreceptors. *Invest. Ophthalmol. Vis. Sci.*, **28**, 1043–1048.
49. Hong, D.H., Pawlyk, B.S., Shang, J., Sandberg, M.A., Berson, E.L. and Li, T. (2000) A retinitis pigmentosa GTPase regulator (RPGR)-deficient mouse model for X-linked retinitis pigmentosa (RP3). *Proc. Natl Acad. Sci. USA*, **97**, 3649–3654.
50. Bavister, B.D. and Andrews, J.C. (1988) A rapid sperm motility bioassay procedure for quality-control testing of water and culture media. *J. In Vitro Fert. Embryo Transf.*, **5**, 67–75.
51. Reed, M.L. and Petters, R.M. (1991) An evaluation of hamster, rat, and mouse sperm-cell motility in media formulated with water of different qualities. *J. In Vitro Fert. Embryo Transf.*, **8**, 41–47.
52. Eppig, J.J. and O'Brien, M.J. (1996) Development *in vitro* of mouse oocytes from primordial follicles. *Biol. Reprod.*, **54**, 197–207.
53. Marín Bivens, C.L., Grøndahl, C., Murray, A., Blume, T., Su, Y.Q. and Eppig, J.J. (2004) Meiosis-activating sterol promotes the metaphase I to metaphase II transition and preimplantation developmental competence of mouse oocytes maturing *in vitro*. *Biol. Reprod.*, **70**, 1458–1464.